J. Fluid Mech. (1976), *vol.* 74, *part* 3, *pp.* 561–591
Printed in Great Britain

Supersonic viscous flow over cones at large angles of attack

By CLIVE A. J. FLETCHER† AND MAURICE HOLT
Department of Mechanical Engineering, University of California, Berkeley

(Received 6 January 1975)

Numerical solutions for the flow field about cones with nose angles of up to 30° at angles of attack up to 50° for a range of Reynolds numbers and wall temperature ratios are presented. The solutions obtained permit interaction between the inviscid region and the boundary layer on the body through the displacement-thickness effect. The solutions are valid throughout the flow field except in the region adjacent to the leeward line of symmetry. Comparisons are made with experimental results and other numerical solutions. Detailed flow structure and the variation of surface conditions with cone angle, incidence, Reynolds number and wall temperature are indicated. The numerical methods used for the inviscid flow equations are Telenin's method and the method of characteristics, while a modified form of the method of integral relations is applied to the boundary-layer equations.

1. Introduction

Supersonic flow about cones at an angle of attack has been the subject of many investigations, both experimental and theoretical. At present experimental data are available for angles of attack up to 30°, cone angles up to 20°, Mach numbers up to 14, and for both laminar and turbulent flow. One of the earliest investigations, for completely laminar flow, was carried out by Tracy (1963). Rainbird (1968) conducted experiments in which the boundary-layer flow was mainly turbulent. More recently, Yahalom (1971) made a comprehensive study of the flow about cones of larger angle (up to 20°).

Previous theoretical investigations have either dealt with purely inviscid flow or have assumed the inviscid solution (theoretical or experimental) at the body to solve the boundary-layer equations. The inviscid flow investigations can be divided into two groups. First, if the cross-flow is everywhere subsonic or just supersonic the governing equations are essentially elliptic in character. Solutions for this case have been obtained by Babenko *et al.* (1965) and by Holt & Ndefo (1970), among others. If the cross-flow has an extensive region of supersonic cross-flow then an internal shock is required in order that the flow can satisfy the boundary condition on the leeward line of symmetry (Fletcher 1975). In this category partial solutions have been obtained by Bazzhin (1970)

† Permanent address: Weapons Research Establishment, Salisbury, South Australia.

and complete solutions by Fletcher (1974*a*, *b*). The shock-capturing method of Kutler & Lomax (1970) is suitable for finding solutions in either of these categories.

Theoretical solutions of the boundary-layer equations on the body have either used calculated inviscid solutions for conditions just outside the boundary layer or experimentally determined conditions at the body surface. The solutions of Bashkin (1968), Dwyer (1971) and Marcillat & Roux (1972) all used numerical inviscid solutions for the appropriate boundary conditions and, consequently, were restricted to conditions for which the cross-flow remains subsonic. Boericke (1971) and Lin & Rubin (1973) mainly used smoothed experimental surface data. Lin & Rubin were able to obtain solutions up to an angle of incidence of 20°.

Solutions for the complete flow field using a modified form of the Navier–Stokes equations (ignoring streamwise diffusion) have been obtained by Lubard & Helliwell (1974). However, it appears that these solutions are restricted to small or moderate incidence.

The present study deals with the supersonic flow about cones at angles of attack which are sufficiently large to guarantee a substantial region of supersonic cross-flow. The solution in the inviscid region is obtained concurrently with the solution in the boundary layer on the body. Interaction between the two regions is permitted through the displacement-thickness effect. This effect is significant and for typical conditions where other investigators have obtained solutions the consequence of not including the displacement-thickness effect is evident. The present method is quite general, so that solutions are not restricted to those particular conditions for which experimental data already exist. The main difference in scope between this and previous investigations is that here solutions have been obtained for angles of attack up to 50° and for cone half-angles up to 30°. The present solutions are valid up to the circumferential station on the leeward side of the cone where interaction begins between the boundary layer and the internal shock. The numerical scheme employed needs to be modified to carry the solutions beyond this station since the cross-flow velocity profiles there are reversed near the cone surface, and indeterminacies are introduced at points where the cross-flow vanishes. Work is now in progress on a revised scheme which overcomes these difficulties and a later paper will deal with the full flow field near the leeward plane of symmetry.

The numerical methods used to solve the inviscid flow equations are Telenin's method (Gilinskii, Telenin & Tinyakov 1964) and the method of characteristics (Fletcher 1974*b*). The numerical method used to solve the boundary-layer equations is an adaptation of the method of integral relations in which the introduction of orthonormal weighting functions permits considerably more accurate solutions to be obtained than were previously possible (Fletcher & Holt 1975).

In §2 the equations of motion used in the inviscid and viscous regions are presented, along with various transformations applied to them. Section 3 describes the boundary and initial conditions appropriate to the different flow regimes. In §4 the different numerical methods used to solve the equations of motion in the various flow regions are briefly described. Section 5 gives details of the interaction mechanism used to connect the boundary-layer and inviscid

regions. Comparisons with Tracy's (1963) experimental data are used to show the effect of the displacement thickness on the heat transfer and pressure distribution. Section 6 gives the main body of numerical results and includes comparison with experimental results, detailed boundary-layer velocity and temperature distributions, and the effect of varying incidence, cone half-angle, Reynolds number and surface temperature on the surface flow parameters; the pressure, skin friction and heat transfer. Since the solutions in the inviscid region for comparable incidences and cone angles are already available (Fletcher 1974*a*), these are not repeated.

2. Equations of motion

2.1. *Inviscid equations*

In the region away from the body surface the flow behaviour is closely approximated by assuming an inviscid non-conducting fluid. If, in addition, the free stream is supersonic and a shock wave is attached to the apex of the cone, the flow variables are independent of the distance x from the cone apex. In terms of spherical co-ordinates (x, θ, ϕ), with corresponding velocity components (u, v, w), the equations of motion are as follows.

Conservation of mass:

$$v_\theta + \frac{1}{\sin\theta} w_\phi + \frac{v}{\rho}\rho_\theta + \frac{w}{\rho \sin\theta}\rho_\phi + 2u + v\cot\theta = 0. \tag{2.1}$$

Conservation of x momentum:

$$vu_\theta + \frac{w}{\sin\theta} u_\phi - (v^2 + w^2) = 0. \tag{2.2}$$

Conservation of θ momentum:

$$vv_\theta + \frac{w}{\sin\theta} v_\phi + \frac{1}{\rho} p_\theta + uv - w^2\cot\theta = 0. \tag{2.3}$$

Conservation of ϕ momentum:

$$vw_\theta + \frac{w}{\sin\theta} w_\phi + \frac{1}{\rho \sin\theta} p_\phi + uw + vw\cot\theta = 0. \tag{2.4}$$

Conservation of energy:

$$\left(vp_\theta + \frac{w}{\sin\theta} p_\phi\right) - a^2\left(v\rho_\theta + \frac{w}{\sin\theta}\rho_\phi\right) = 0. \tag{2.5}$$

The variables in (2.1)–(2.5) have been made dimensionless using a^*, the critical sound speed, and ρ_∞, the free-stream density. The character of the equations is determined by the magnitude of the cross-flow Mach number

$$M_{cr} = \{(v^2 + w^2)/a^2\}^{\frac{1}{2}}.$$

When $M_{cr} < 1$ the equations are elliptic in character and require appropriate boundary conditions. This is the situation in the region adjacent to the wind-

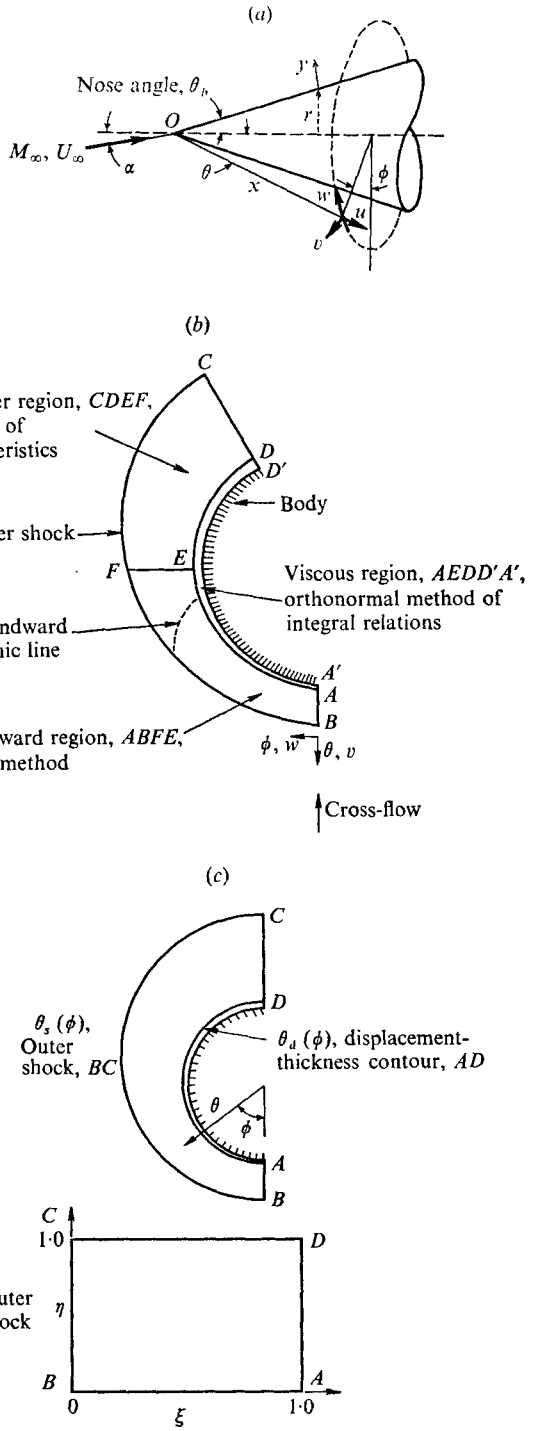

FIGURE 1. (*a*) Co-ordinate system and velocities. (*b*) Classification of the different flow regions on the basis of the numerical method used. (*c*) Co-ordinate transformation used in the inviscid regions; $\xi = (\theta_s - \theta)/(\theta_s - \theta_d)$, $\eta = \phi/\pi$.

ward line of symmetry (see figure 1*b*) and extending circumferentially for approximately 80° on either side of this line. The exact extent of this region depends on the particular choice of the external parameters: the free-stream Mach number M_∞, the incidence angle α and the cone half-angle θ_b. When $M_{cr} > 1$ the equations are hyperbolic in character. The external parameters M_∞, α and θ_b have been chosen such that the hyperbolic region extends from the sonic line to some undetermined circumferential location adjacent to the leeward line of symmetry. The hyperbolic region will be terminated by an internal shock.

In order to simplify the procedure for solving (2.1)–(2.5), the region bounded by the windward line of symmetry, the displacement-thickness profile, the leeward line of symmetry and the outer shock is transformed into a rectangle by introducing new independent variables ξ and η:

$$\xi = \frac{\theta_s(\phi)-\theta}{\theta_s(\phi)-\theta_d(\phi)}, \quad \eta = \phi/\pi. \tag{2.6}$$

Here $\theta_s(\phi)$ is the outer shock profile and $\theta_d(\phi)$ is the displacement-thickness profile. The resulting equations and further details may be found in Fletcher (1974*a*).

2.2. *Viscous equations*

Close to the body it is assumed that viscous effects can be completely accounted for using the three-dimensional compressible boundary-layer equations. For a general inclined axisymmetric body these equations are the following.

Conservation of mass:

$$\frac{\partial}{\partial x}(\rho u r)+\frac{\partial}{\partial y}(\rho v r)+\frac{1}{r}\frac{\partial}{\partial \phi}(\rho w r) = 0. \tag{2.7}$$

Conservation of x momentum:

$$\rho u\frac{\partial u}{\partial x}+\rho v\frac{\partial u}{\partial y}+\frac{\rho w}{r}\frac{\partial u}{\partial \phi}-\frac{\rho w^2}{r}\frac{\partial r}{\partial x} = -\frac{\partial p_e}{\partial x}+\frac{\partial}{\partial y}\left(\mu\frac{\partial u}{\partial y}\right). \tag{2.8}$$

Conservation of ϕ momentum:

$$\rho u\frac{\partial w}{\partial x}+\rho v\frac{\partial w}{\partial y}+\frac{\rho w}{r}\frac{\partial w}{\partial \phi}+\frac{\rho u w}{r}\frac{\partial r}{\partial x} = -\frac{1}{r}\frac{\partial p_e}{\partial \phi}+\frac{\partial}{\partial y}\left(\mu\frac{\partial w}{\partial y}\right). \tag{2.9}$$

Conservation of energy:

$$\rho u\frac{\partial H_T}{\partial x}+\rho v\frac{\partial H_T}{\partial y}+\frac{\rho w}{r}\frac{\partial H_T}{\partial \phi} = \frac{1}{Pr}\frac{\partial}{\partial y}\left(\mu\frac{\partial H_T}{\partial y}\right)+\left(1-\frac{1}{Pr}\right)\frac{\partial}{\partial y}\left\{\mu\frac{\partial}{\partial y}\tfrac{1}{2}(u^2+w^2)\right\}, \tag{2.10}$$

where H_T, the total enthalpy, is given by

$$H_T = C_p T+\tfrac{1}{2}(u^2+w^2). \tag{2.11}$$

A subscript e indicates external conditions, i.e. the inviscid solution at the displacement-thickness contour.

In (2.7)–(2.11) dimensionless variables have been introduced by using suitable combinations of a^*, ρ_∞ and L, a suitable reference length.

Equations (2.7)–(2.11) can be simplified by making the following transformations in turn.

(*a*) The Howarth transformation (to remove explicit dependence on the density):

$$x_1 = x, \quad y_1 = \left(\frac{p_\infty}{p_e}\right)^{\frac{1}{2}} \int_0^y \rho\, dy, \quad \phi_1 = \phi. \tag{2.12}$$

(*b*) The Mangler transformation (to reduce the effect of r):

$$x_2 = \int_0^{x_1} r^2 dx, \quad y_2 = r y_1, \quad \phi_2 = \phi_1. \tag{2.13}$$

(*c*) The Blasius transformation (to reduce the number of independent variables from three to two):

$$\eta = \left(\frac{u_\infty}{2\mu_\infty}\right)^{\frac{1}{2}} \frac{y_2}{x_2^{\frac{1}{2}}}, \quad \zeta = \phi_2. \tag{2.14}$$

The above approach essentially follows Dwyer (1971). Application of the above transformations to (2.7)–(2.11) produces the following.

Conservation of mass:

$$\frac{1}{\sin\theta_b}\frac{\partial w_2}{\partial \zeta} + \frac{\partial v_2}{\partial \eta} = -\frac{w_2}{\sin\theta_b}\left\{\frac{p_{e\zeta}}{2p_e} + \frac{u_{e\zeta}}{u_e}\right\} - 1{\cdot}5u_2. \tag{2.15}$$

Conservation of x momentum:

$$\frac{w_2}{\sin\theta_b}\frac{\partial u_2}{\partial \zeta} + v_2\frac{\partial u_2}{\partial \eta} = l_2\frac{\partial^2 u_2}{\partial \eta^2} - w_2\left\{\frac{u_2}{\sin\theta_b}\frac{u_{e\zeta}}{u_e} - w_2\right\}. \tag{2.16}$$

Conservation of ϕ momentum:

$$\frac{w_2}{\sin\theta_b}\frac{\partial w_2}{\partial \zeta} + v_2\frac{\partial w_2}{\partial \eta} = -\left[\frac{B}{u_e^2}(1-s) - \tfrac{1}{2}(u_2^2 + w_2^2)\right] \times \frac{\gamma - 1}{\gamma \sin\theta_b}\frac{p_{e\zeta}}{p_e} + l_2\frac{\partial^2 w_2}{\partial \eta^2} - w_2\left\{\frac{w_2}{\sin\theta_b}\frac{u_{e\zeta}}{u_e} + u_2\right\}. \tag{2.17}$$

Conservation of energy

$$\frac{w_2}{\sin\theta_b}\frac{\partial s}{\partial \zeta} + v_2\frac{\partial s}{\partial \eta} = l_3\frac{\partial^2 s}{\partial^2 \eta} + l_4\frac{\partial^2}{\partial \eta^2}\{\tfrac{1}{2}(u_2^2 + w_2^2)\}. \tag{2.18}$$

Here $u_2 = u/u_e$, $w_2 = w/u_e$,

$$v_2 = \frac{(1{\cdot}5)^{\frac{1}{2}} Re_r^{\frac{1}{2}}}{u_e \sin^{\frac{1}{2}}\theta_b}\left(\frac{p_\infty}{p_e}\right)^{\frac{1}{2}}\left[\rho v + u\int_0^y \frac{\partial \rho}{\partial x}dy + \frac{w}{r}\int_0^y \frac{\partial \rho}{\partial \phi}dy\right] - \tfrac{1}{2}\eta\left[u_2 + \frac{w_2}{\sin\theta_b}\frac{p_{e\zeta}}{p_e}\right],$$

$$l_2 = \frac{1{\cdot}5C}{u_e}\left[\frac{\gamma - 1}{\gamma + 1} + \frac{2}{(\gamma+1)M_\infty^2}\right]^{-\frac{1}{2}},$$

$$l_3 = l_2/Pr, \quad l_4 = \frac{u_e^2}{B} l_2\left\{\frac{1}{Pr} - 1\right\}$$

and

$$\mu/\mu_\infty = C\,T/T_\infty.$$

To simplify the introduction of the method of integral relations the Crocco transformation is applied. This replaces the independent variables ζ and η by $\bar{\zeta}$ and u_2 (the subscript 2 will be dropped henceforth), i.e.

$$\bar{\zeta} = \zeta, \quad u = \int_0^\eta \tau d\eta, \tag{2.19}$$

where $\tau = \partial u/\partial\eta$ and is proportional to the shear stress in the radial direction. The equations in Crocco form are similar to (2.15)–(2.18) and, consequently, are not shown explicitly.

The method of integral relations seeks weighted combinations of (2.15)–(2.18) such that explicit dependence on v_2 disappears. This is clearly desirable since v_2 has no immediate physical significance. If (2.15) is multiplied by $g_k(u)$ and added to $g_k'(u) \times (2.16)$, application of the Crocco transformation to the combination and integration with respect to u from 0 to 1 produce the result

$$\frac{\partial}{\partial\zeta}\int_0^1 g_k \frac{w}{\tau} du = \sin\theta_b \Big[l_5 \int_0^1 g_k \frac{w}{\tau} du - 1{\cdot}5 \int_0^1 g_k \frac{u}{\tau} du - l_2 \{g_k' \tau\}_{\text{wall}} - l_2 \int_0^1 g_k'' \tau du - \int_0^1 g_k' \frac{w}{\tau} \Big(u \frac{w_e}{u_e} - w \Big) du \Big]. \tag{2.20}$$

Similarly, by taking $wg_k \times (2.15) + wg_k' \times (2.16) + g_k \times (2.17)$, applying the Crocco transformation and integrating, the following expression results:

$$\begin{aligned} \frac{\partial}{\partial\zeta}\int_0^1 g_k \frac{w^2}{\tau} du = \sin\theta_b \Big[& l_7 \int_0^1 g_k \frac{w^2}{\tau} du - 2{\cdot}5 \int_0^1 g_k \frac{uw}{\tau} du \\ & - l_2 \int_0^1 g_k'' \tau w du - 2l_2 \int_0^1 g_k' \tau \frac{\partial w}{\partial u} du \\ & - \int_0^1 g_k' \frac{w^2}{\tau} \Big(u \frac{w_e}{u_e} - w \Big) du + l_6 \frac{B}{u_e^2} \int_0^1 g_k \frac{(1-s)}{\tau} du \\ & - l_2 \Big(g_k \frac{\partial w}{\partial u} \tau \Big)_{\text{wall}} + l_8 \int_0^1 g_k \frac{u^2}{\tau} du \Big]. \end{aligned} \tag{2.21}$$

Also, by taking $sg_k \times (2.15) + sg_k' \times (2.16) \times g_k + (2.18)$, applying the Crocco transformation and integrating, the following expression is obtained:

$$\begin{aligned} \frac{\partial}{\partial\zeta}\int_0^1 g_k \frac{sw}{\tau} du = \sin\theta_b \Big[& l_5 \int_0^1 g_k \frac{sw}{\tau} du - 1{\cdot}5 \int_0^1 g_k \frac{su}{\tau} du \\ & - l_2 \{g_k' s\tau\}_{\text{wall}} - l_2 \int_0^1 g_k'' \tau s du - (l_2 + l_3) \int_0^1 g_k' \tau \frac{\partial s}{\partial u} du \\ & - \int_0^1 g_k' \frac{sw}{\tau} \Big(u \frac{w_e}{u_e} - w \Big) du - l_3 \Big(g_k \frac{\partial s}{\partial u} \tau \Big)_{\text{wall}} - l_4 \int_0^1 g_k' \tau \Big(u + \frac{\partial w}{\partial u} w \Big) du \Big]. \end{aligned} \tag{2.22}$$

In (2.20)–(2.22) the total enthalpy H_T has been replaced by s, defined as

$$s = 1 - H_T/B, \tag{2.23}$$

where B, the Bernoulli constant, is given by $B = \frac{1}{2}(\gamma+1)/(\gamma-1)$. The expression for B follows from the reduction to dimensionless form. s has the desirable

property of vanishing at the outer edge of the boundary layer. At the wall $s = s_w = 1 - T_w/T_0$, where T_0 is the stagnation temperature. In (2.20)–(2.22) the weighting functions $g_k(u)$ have the following form:

$$g_k(u) = \sum_{k=1}^{j} b_{kj}(1-u)^k. \tag{2.24}$$

The coefficients b_{kj} are evaluated using the Gram–Schmidt orthonormalization process. A further discussion of the orthonormal method of integral relations may be found in Fletcher & Holt (1975).

In (2.20)–(2.22) the coefficients l_1, l_2, l_3, etc., depend primarily on the inviscid conditions. Those not already defined are given by

$$l_5 = -\left\{\frac{p_{e\xi}}{2p_e \sin\theta_b} + \frac{w_e}{u_e}\right\},$$

$$l_6 = -\frac{\gamma-1}{\gamma \sin\theta_b}\frac{p_{e\xi}}{p_e},$$

$$l_7 = -\left\{\frac{1}{\gamma}\frac{p_{e\xi}}{2p_e \sin\theta_b} + 2\frac{w_e}{u_e}\right\},$$

$$l_8 = \frac{\gamma-1}{\gamma}\frac{p_{e\xi}}{2p_e \sin\theta_b}.$$

As this point it may be noted that (2.20)–(2.22) contain no approximations other than those inherent in the boundary-layer equations (2.7)–(2.10).

3. Boundary conditions and initial conditions

3.1. *Inviscid flow region*

The boundary conditions on the windward line of symmetry are that w and $\partial u/\partial\phi$, $\partial v/\partial\phi$, $\partial\rho/\partial\phi$ and $\partial p/\partial\phi$ are zero. At the outer shock (unknown in advance) the conditions inside the shock are given in terms of the free-stream conditions by the Rankine–Hugoniot relations (see Fletcher 1974*a*). At the inner surface ($\xi = 1$) zero flow normal to the displacement-thickness contour is required. The precise location of the displacement-thickness contour is determined as part of the interaction process (see §5). In addition, the hyperbolic region requires initial conditions on some non-characteristic line. This line turns out to be the extreme downstream edge (in the cross-flow direction) of the elliptic region (see §4).

3.2. *Viscous flow region*

At the body surface $u = v = w = 0$ and $T = T_w$. At the outer edge of the boundary layer the inviscid solution gives p_e, u_e, w_e, $p_{e\phi}$ and $w_{e\phi}$. The initial conditions on the windward line of symmetry, required before (2.20)–(2.22) can be solved, are obtained by noting that (2.20)–(2.22) reduce at $\phi = 0$ to the following algebraic equations:

$$\int_0^1 g_k \frac{w_\zeta}{\tau}\,du = \sin\theta_b\left[-1{\cdot}5\int_0^1 g_k\frac{u}{\tau}\,du - l_2\{g_k'\tau\}_{\text{wall}} - l_2\int_0^1 g_k''\tau\,du\right], \tag{3.1}$$

$$\int_0^1 g_k \frac{w_\zeta^2}{\tau} du = \frac{\sin\theta_b}{2}\Big[-2{\cdot}5\int_0^1 g_k \frac{u w_\zeta}{\tau} du - l_2 \int_0^1 \tau w_\zeta g_k'' du$$
$$- 2l_2 \int_0^1 g_k' \frac{\partial w_\zeta}{\partial u} \tau du + l_9 \int_0^1 \frac{g_k}{\tau}(1-s)\, du$$
$$- l_{10} \int_0^1 g_k \frac{u^2}{\tau} du - l_2 \left\{ g_k \tau \frac{\partial w_\zeta}{\partial u} \right\}_{\text{wall}} \Big] \tag{3.2}$$

and

$$\int_0^1 g_k \frac{s w_\zeta}{\tau} du = \sin\theta_b \Big[-1{\cdot}5 \int_0^1 g_k \frac{su}{\tau} du - \left(\frac{1}{Pr}+1\right) l_2 \int_0^1 g_k' \tau \frac{\partial s}{\partial u} du - l_2 \int_0^1 \tau s g_k'' du$$
$$- l_4 \int_0^1 g_k' \tau u\, du - l_2 \{ s g_k' \tau \}_{\text{wall}} - l_3 \left\{ g_k \frac{\partial u}{\partial s} \tau \right\}_{\text{wall}} \Big], \tag{3.3}$$

where
$$l_9 = -\frac{\gamma-1}{\gamma} \frac{B}{u_e^2} \frac{p_{e\zeta\zeta}}{p_e \sin\theta_b},$$
$$l_{10} = \frac{\gamma-1}{\gamma} \frac{p_{e\zeta\zeta}}{2 p_e \sin\theta_b}.$$

Equation (3.2) is obtained from (2.21) by differentiating with respect to ζ.

In order to simplify the solution of (3.1)–(3.3) the following algebraic representations for the functions w_ζ/τ, w_ζ^2/τ and $s w_\zeta/\tau$ are introduced:

$$z_1 = w_\zeta/\tau = \left\{ c_{01} + \sum_{j=1}^{N-1} c_{j1} g_j(u) \right\} \Big/ (1-u), \tag{3.4a}$$

$$z_2 = w_\zeta^2/\tau = \left\{ c_{02} + \sum_{j=1}^{N-1} c_{j2} g_j(u) \right\} \Big/ (1-u), \tag{3.4b}$$

$$z_3 = s w_\zeta/\tau = \left\{ c_{03} + \sum_{j=1}^{N-1} c_{j3} g_j(u) \right\} \Big/ (1-u). \tag{3.4c}$$

Once the coefficients c_{j1} have been determined, w_ζ, τ and s follow since the $g_j(u)$ are known *a priori*. Certain of the coefficients may be obtained by satisfying the boundary conditions. At the outer edge of the boundary layer $s = 0$ and $g_j(1) = 0$ for all j. Hence

$$c_{03} = 0. \tag{3.5a}$$

Also $w_{e\zeta}/u_e = z_2/z_1 = c_{02}/c_{01}$, thus

$$c_{02} = (w_{e\zeta}/u_e)\, c_{01}. \tag{3.5b}$$

At the body surface $u = 0$, $w_\zeta = 0$ and $s = s_w$ (given, *a priori*). Thus

$$c_{0i} + \sum_{j=1}^{N-1} c_{j1} g_j(0) = 0, \quad i = 1, 2, 3, \tag{3.6a–c}$$

$$\sum_{j=1}^{N-1} c_{j2} g_j'(0) = 0 \tag{3.7}$$

and
$$\sum_{j=1}^{N-1} c_{j3} g_j'(0) = s_w \sum_{j=1}^{N-1} c_{j1} g_j'(0). \tag{3.8}$$

Seven of the coefficients c_{ji} may be determined from the boundary conditions above. The other $3N-7$ coefficients are determined from (3.1)–(3.3). Substitution

of the expressions (3.4) into (3.1)–(3.3) permits the following simple representation for (3.1)–(3.3):

$$c_{01}SF_k + c_{k1} = S_{k1}, \quad k = 1, \ldots, N-2, \tag{3.9a}$$

$$c_{02}SF_k + c_{k2} = S_{k2}, \quad k = 1, \ldots, N-3, \tag{3.9b}$$

$$c_{k3} = S_{k3}, \quad k = 1, \ldots, N-2, \tag{3.9c}$$

where

$$SF_k = \int_0^1 [g_k(u)/(1-u)]\,du \tag{3.9d}$$

and S_{ki} is the right-hand side of (3.1)–(3.3) evaluated numerically. The integrals in (3.1)–(3.3) and (3.9d) have been evaluated using a local Simpson's rule and m evaluations of the integrand across the boundary layer (typically $m = 32$). The simple form of the left-hand sides of (3.9a–c) follows from the particular choice of the orthonormal weighting functions $g_k(u)$ (see Fletcher & Holt 1975). Equations (3.5)–(3.9) constitute $3N$ equations for the $3N$ unknown coefficients c_{ji}.

The problem must be solved iteratively because the terms S_{ki} cannot be evaluated until w_ζ, τ and s and hence z_1, z_2 and z_3 have been evaluated. To simplify the process (3.9a–c) are written as

$$E_k = c_{01}SF_k + c_{k1} - S_{k1} = 0, \tag{3.10a}$$

$$F_k = c_{02}SF_k + c_{k2} - S_{k2} = 0, \tag{3.10b}$$

$$G_k = c_{k3} - S_{k3} = 0. \tag{3.10c}$$

An arbitrary choice of the coefficients c_{ji} will make E_k, F_k and G_k non-zero. The iterative technique is based on a function minimization method due to Powell (1964). Powell's method seeks to modify the current values of c_{ji} until

$$H = \sum_{j=1}^{N-2} E_k^2 + \sum_{j=1}^{N-3} F_k^2 + \sum_{j=1}^{N-2} G_k^2 = 0. \tag{3.11}$$

The major difficulty with this approach lies in choosing the initial estimates of the c_{ji} with sufficient accuracy to ensure convergence of the process. This problem is made tractable in the following manner. If a solution has been found for a particular value of N this solution may be used as the first approximation to the solution of order $N+1$. The three extra coefficients c_{Ni} are initially set equal to zero, consequently the only contributions, initially, to H are from E_{N-1}, F_{N-2} and G_{N-1}. This technique has worked quite satisfactorily and essentially reduces the problem of choosing suitable starting values for the c_{ji}'s to that for the lowest-order solution sought. If (3.2) is temporarily ignored a solution with $N = 3$ may be obtained. In this case (3.1) and (3.3) give one relationship each when $k = 1$. For this case suitable starting values for w_ζ/τ, w_ζ^2/τ and sw_ζ/τ at $u = 0{\cdot}5$ are guessed. Then (3.4) give corresponding values of the c_{ji}'s. Once a solution satisfying (3.11) has been found the order N is increased by one and the process repeated. This is continued until a solution is obtained at $N = 7$. All the solutions presented in this paper are for $N = 7$ and $m = 32$. This choice is considered a reasonable compromise between accuracy and computer execution time on the basis of the results for a cone at zero angle of attack (Fletcher & Holt 1975).

The solution giving the values of the c_{ji} for $N = 7$ can be used to obtain z_1, z_2 and z_3 [using (3.4)] and hence w_ζ, τ and s on the windward line of symmetry,

$\zeta = 0$. However, as will be indicated in §4, the solutions for the c_{ji} can be used directly as initial data for coefficients in a series representation [equivalent to (3.4)] for w, τ and s appropriate to the solution for the region $\zeta > 0$.

4. Solution of the equations of motion

4.1. *Inviscid region*

For the purposes of obtaining numerical solutions the inviscid region is split up into two regions (see figure 1*b*), *ABFE* and *CDEF*. In the windward region *ABFE*, Telenin's method (Gilinskii *et al.* 1964) is used. In this the equations of motion (2.1)–(2.5) are treated as ordinary differential equations in ξ [see (2.6)] and are integrated along *BA*, *FE* and three equally spaced rays between *BA* and *FE*, from the outer shock to the body. Since the outer shock is not known *a priori* the method is iterative. Powell's (1964) method is used to modify the outer-shock location *BF* until the normal velocities on *AE*, the displacement-thickness contour, are zero. Further details may be obtained from Fletcher (1974*a*).

The solution on the last ray, *FE*, which is deliberately chosen to lie beyond the windward sonic line, is used to give initial data for a characteristics solution. The line *FE* is normally positioned at $\phi = 90°$. However, for some of the large incidence data (e.g. $\alpha = 50°$, $\theta_b = 10°$) the sonic line is closer to the windward symmetry line and *FE* is located at $\phi = 72°$. For the case $\alpha = 12°$, $\theta_b = 10°$, *FE* is located at $\phi = 110°$.

In the shoulder region *CDEF*, the upstream interpolation method of characteristics, due to Belotserkovskii & Chushkin (1965), has been followed. This method retains a fixed grid rather than permitting the grid to be defined by the characteristics development. Values of the flow variables at the downstream mesh points are obtained by projecting the characteristic lines through the mesh point in the upstream direction until they intersect the previous line (constant η) of known data. At the intersections the local function values can be obtained by interpolating among adjacent points in the ξ direction. The compatibility conditions connect the upstream interpolated values with the unknown values at the downstream mesh point. Further details may be found in Fletcher (1974*a*).

4.2. *Viscous region*

In the region *AEDD'A*, adjacent to the body (figure 1*b*), the equations of motion (2.20)–(2.22) are solved using the orthonormal method of integral relations. The following representation for w/τ, w^2/τ and sw/τ is introduced:

$$y_1 = \frac{w}{\tau} = \left\{b_{01} + \sum_{j=1}^{N-1} b_{j1} g_j(u)\right\} \Big/ (1-u), \tag{4.1a}$$

$$y_2 = \frac{w^2}{\tau} = \left\{b_{02} + \sum_{j=1}^{N-1} b_{j2} g_j(u)\right\} \Big/ (1-u), \tag{4.1b}$$

$$y_3 = \frac{sw}{\tau} = \left\{b_{03} + \sum_{j=1}^{N-1} b_{j3} g_j(u)\right\} \Big/ (1-u). \tag{4.1c}$$

Seven of the unknown coefficients b_{ji} may be determined from the following boundary conditions:

(*a*) $s = 0$ at $u = 1$, which leads to $b_{03} = 0$; (4.2*a*)

(*b*) $w_e/u_e = y_2/y_1$ at $u = 1$, which leads to $b_{02} = (w_e/u_e)\,b_{01}$; (4.2*b*)

(*c*) $y_1, y_2, y_3, w = 0$ at $u = 0$,

which leads to
$$b_{0i} + \sum_{j=1}^{N-1} b_{ji} g_j(0) = 0, \quad i = 1, 2, 3, \tag{4.2c–e}$$
$$\sum_{j=1}^{N-1} b_{j2} g_j'(0) = 0; \tag{4.2f}$$

(*d*) $s = s_w$ at $u = 0$, which leads to
$$\sum_{j=1}^{N-1} b_{j3} g_j'(0) = s_w \sum_{j=1}^{N-1} b_{j1} g_j'(0), \tag{4.2g}$$

where
$$s_w = 1 - T_w/T_0. \tag{4.3}$$

Introduction of (4.1) into (2.20)–(2.22) produces the following result:
$$SF_k \frac{\partial b_{01}}{\partial \zeta} + \frac{\partial b_{k1}}{\partial \zeta} = T_{k1}, \quad k = 1, \ldots, N-2, \tag{4.4a}$$
$$SF_k \frac{\partial b_{02}}{\partial \zeta} + \frac{\partial b_{k2}}{\partial \zeta} = T_{k2}, \quad k = 1, \ldots, N-3, \tag{4.4b}$$
$$\partial b_{k3}/\partial \zeta = T_{k3}, \quad k = 1, \ldots, N-2, \tag{4.4c}$$

where SF_k is given by (3.9*d*) and the T_{ki} are the numerical values of the right-hand sides of (2.20)–(2.22). Equations (4.4) can be integrated if $\partial b_{ki}/\partial \zeta$ can be expressed explicitly. In general
$$b_{ki}^{n+1} = b_{ki}^n + h\,\partial b_{ki}^n/\partial \zeta, \tag{4.5}$$

where h is the step size in the ζ direction. Clearly b_{ki}^n and b_{ki}^{n+1} both satisfy the boundary conditions (4.2). Consequently the following boundary conditions for $\partial b_{ki}/\partial \zeta$ may be obtained:
$$\partial b_{03}/\partial \zeta = 0, \tag{4.6a}$$
$$\frac{\partial b_{02}}{\partial \zeta} = b_{01} \frac{\partial}{\partial \zeta}\left(\frac{w_e}{u_e}\right) + \frac{w_e}{u_e} \frac{\partial b_{01}}{\partial \zeta}, \tag{4.6b}$$
$$\frac{\partial b_{01}}{\partial \zeta} + \sum_{j=1}^{N-1} \frac{\partial b_{ji}}{\partial \zeta} g_j(0) = 0, \tag{4.6c–e}$$
$$\sum_{j=1}^{N-1} \frac{\partial b_{j2}}{\partial \zeta} g_j'(0) = 0 \tag{4.6f}$$

and
$$\sum_{j=1}^{N-1} \frac{\partial b_{j3}}{\partial \zeta} g_j'(0) = s_w \sum_{j=1}^{N-1} \frac{\partial}{\partial \zeta} b_{j1} g_j'(0). \tag{4.6g}$$

Combination of (4.4*a*, *c*) and (4.6*c*, *e*, *g*) produces the following explicit expression for $\partial b_{01}/\partial \zeta$:
$$\frac{\partial b_{01}}{\partial \zeta} = \sum_{k=1}^{N-2} \left\{T_{k1} - \frac{T_{k3}}{s_w}\right\} E_{wk} \Big/ \left\{1 + \sum_{k=1}^{N-2} SF_k E_{wk}\right\}, \tag{4.7}$$

where
$$E_{wk} = g_k'(0) - \frac{g_{N-1}'(0)}{g_{N-1}(0)} g_k(0). \tag{4.7a}$$

$\partial b_{02}/\partial\zeta$ then follows from (4.6*b*), and substitution for $\partial b_{01}/\partial\zeta$ and $\partial b_{02}/\partial\zeta$ permits explicit evaluation of $\partial b_{k1}/\partial\zeta$ and $\partial b_{k2}/\partial\zeta$ using (4.4*a*, *b*).

The expression for $\partial b_{ki}/\partial\zeta$ cannot be integrated from $\zeta = 0$ since $w = 0$ there and this causes difficulty in trying to invert (4.1) to find w, τ and s. At a small distance ϵ beyond $\zeta = 0$ the solution for y_i may be obtained from §3.2 by noting that

$$b_{k1} = \epsilon C_{k1}, \quad b_{k2} = \epsilon^2 C_{k2}, \quad b_{k3} = \epsilon C_{k3}. \tag{4.8}$$

The value of ϵ used in the present study was $0{\cdot}005\,\pi$ rad.

Equations (4.4) and related equations have been integrated in the windward region using a generalized predictor–corrector technique due to Gear (1971) in which the step size and order of the predictor–corrector are chosen to suit a specified relative error. In the present study a relative error of 10^{-4} was used. Preliminary tests indicated that reducing the relative error below 10^{-4} produced no change in the solution. The step size varied between 0·001 and 0·1 rad.

In the shoulder region a second-order predictor scheme has been used with a typical step size of $0{\cdot}0004\,\pi$. The second-order predictor was chosen to be consistent with the accuracy of the solution in the inviscid shoulder region. The relatively small step size was necessary for stability.

4.3. *Comments on extension of the method to the far windward region*

The procedure described in §4.2 runs into difficulties when the cross-flow profile reverses, as on the far windward side of the cone (beyond the cross-flow separation point). In this region, at each station ζ = constant, $w = 0$ at a point within the boundary layer and (4.1*a–c*) give indeterminate values of τ and s. Thus, at such points, it is not possible to evaluate the integrals on the right sides of (2.20)–(2.22). To overcome this problem it is necessary to represent all the combinations of w, τ, s and $\partial w/\partial u$ by series of type (4.1). The coefficients in these are connected by algebraic relations in terms of values of w, τ and s at various stations u = constant. Full details will be presented in a later paper.

5. Viscous/inviscid interaction

As long as the flow remains attached it is customary to assume that the retardation of the flow in the boundary layer adjacent to the body surface has a negligible effect on the outer inviscid flow. However, previous studies indicate that boundary-layer solutions based on experimental pressure distributions are generally more accurate than those based on inviscid solutions (Boericke 1971).

Since the present study has been concerned with external conditions

$$(M_\infty, \alpha, \theta_b, Re_x, T_w/T_0)$$

for which no experimental data exist, it has been necessary to rely on an inviscid solution (Fletcher 1974*b*). Also, the large angles of attack considered here have resulted in relatively thick boundary layers on the leeward side of the cone. Therefore the inviscid solutions (Fletcher 1974*b*) have been modified to include the displacement-thickness effect of the boundary layer on the outer flow. The

resulting modified solutions for u_e, w_e, ρ_e and p_e at the displacement-thickness contour have then been used to recompute the boundary-layer solution.

A basic assumption underlying the solution in the inviscid region is that the flow is conical, i.e. that any boundary of the flow, such as the displacement-thickness contour, will grow linearly with x. A basic assumption underlying the solution of the boundary-layer equations is that any flow parameter, such as the displacement-thickness contour, varies like $x^{\frac{1}{2}}$ (after Moore 1951). The value of these two assumptions is that they both permit a problem with three independent variables to be reduced to a problem in two independent variables.

Once the displacement thickness is permitted to modify the outer inviscid flow an inconsistency arises in that the displacement thickness appears to grow like x or $x^{\frac{1}{2}}$, depending on the frame of reference. This inconsistency is overcome here by introducing the concept of a 'locally conical' outer flow. That is, at any particular x (and Re_x), the flow field is assumed to behave as though it were bounded on the inside by a semi-infinite conical body whose local radius coincides with the local displacement-thickness contour and whose apex coincides with the apex of the original body. This represents an approximation in which terms in the governing equation involving radial derivatives (associated with the non-conical inner boundary to the inviscid region) are taken to be negligibly small compared with other terms.

An implicit expression for the displacement thickness δ_d has been given by Moore (1952) as

$$1{\cdot}5\rho_e u_e \sin\theta_b(\delta_d - \delta_x) + \partial[\rho_e w_e(\delta_d - \delta_\phi)]/\partial\phi = 0, \tag{5.1}$$

where

$$\frac{\delta_x}{x} = [p_e/(1{\cdot}5 Re_x p_\infty)]^{\frac{1}{2}} \int_0^1 \frac{(1-u\rho/\rho_e)}{\rho\tau}\, du$$

and

$$\frac{\delta_\phi}{x} = [p_e/(1{\cdot}5 Re_x p_\infty)]^{\frac{1}{2}} \int_0^1 \frac{\left(1-\dfrac{\rho}{\rho_e}\dfrac{w}{w_e}u_e\right)}{\rho\tau}\, du.$$

For the rest of the paper, $\delta_1 \equiv \delta_d/x$ will be referred to as the displacement thickness. The details of the interaction depend on whether the outer flow is governed by elliptic or hyperbolic equations.

5.1. *Windward region*

The numerical solution of the inviscid flow in the windward region (see figure 1*b*) is obtained using Telenin's method, which is suitable for elliptic or mixed conditions. Solutions are sought along five rays normal to the cone surface. Intermediate values of u_e, w_e, etc. required by the boundary-layer solution are obtained by interpolation.

Initially the displacement thickness $\delta_{1\mathrm{inv}}$ and displacement-thickness slope $[\partial\delta_1/\partial\zeta]_{\mathrm{inv}}$ are assumed to be zero. An inviscid solution and a boundary-layer solution up to FE (in figure 1*b*) are then obtained. A new inviscid displacement thickness is chosen as follows:

$$\delta_{1\,\mathrm{inv}}^{n+1} = \delta_{1\,\mathrm{inv}}^{n} + k_e(\delta_{1\,\mathrm{visc}}^{n} - \delta_{1\,\mathrm{inv}}^{n}). \tag{5.2}$$

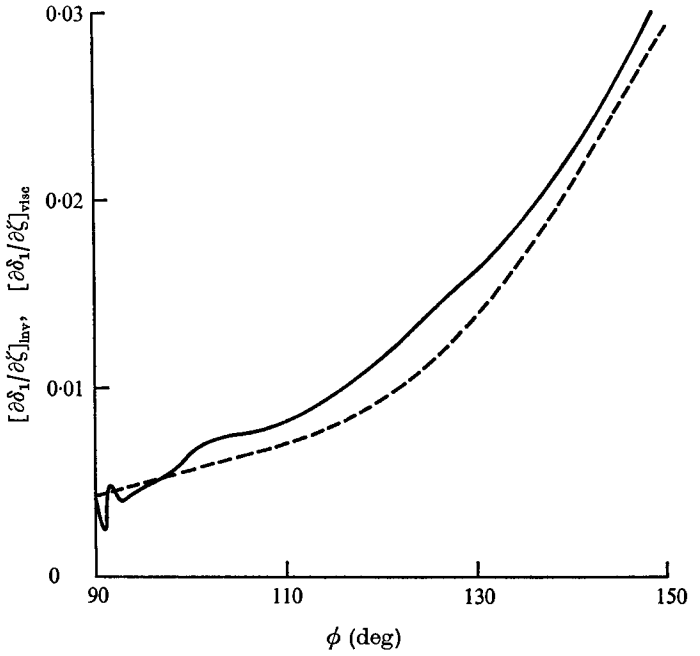

FIGURE 2. Growth of displacement-thickness slope. $M_\infty = 7$, $\theta_b = 20°$, $\alpha = 30°$, $Re_x = 5\times10^5$, $T_w/T_0 = 0{\cdot}40$. ———, $[\partial\delta_1/\partial\zeta]_{\rm visc}$; – – – –, $[\partial\delta_1/\partial]_{\rm inv}$.

A new displacement-thickness slope is chosen similarly. k_e is a factor, chosen empirically to equal 0·8. At each step of the iteration a fresh inviscid solution and a fresh boundary-layer solution are calculated. The procedure is continued until $\delta_{1\,\rm visc}^{n+1}$ and $(\partial\delta_1^{n+1}/\partial\zeta)_{\rm visc}$ are in acceptable agreement with $\delta_{1\,\rm inv}^{n+1}$ and $\partial\delta_{1\,\rm inv}^{n+1}/\partial\zeta$. Typically this takes three iterations.

5.2. *Shoulder region*

The governing inviscid equations are hyperbolic in character in the shoulder region (see figure 1*b*). Since the boundary-layer equations are parabolic it is convenient to permit solutions in the inviscid and viscous regions to develop simultaneously without the need for any global iteration.

The solution at the $(i+1)$th mesh point (in the ζ direction) is derived from the solution up to the ith mesh point in the following manner.

(1) The inviscid displacement-thickness slope is extrapolated to the $(i+1)$th mesh point according to

$$\left.\frac{\partial\delta_1^*}{\partial\zeta}\right|_{\rm inv} = \left.\frac{3}{2}\frac{\partial\delta_1^i}{\partial\zeta}\right|_{\rm inv} - \left.\frac{1}{2}\frac{\partial\delta_1^{i-1}}{\partial\zeta}\right|_{\rm inv}. \tag{5.3}$$

(2) An inviscid solution is obtained at the $(i+1)$th mesh point.

(3) The inviscid solution provides boundary conditions to permit the boundary-layer solution to be integrated to the $(i+1)$th mesh point.

(4) $\delta_1^{i+1}|_{\rm visc}$ and $[\partial\delta_1^{i+1}/\partial\zeta]_{\rm visc}$ are computed.

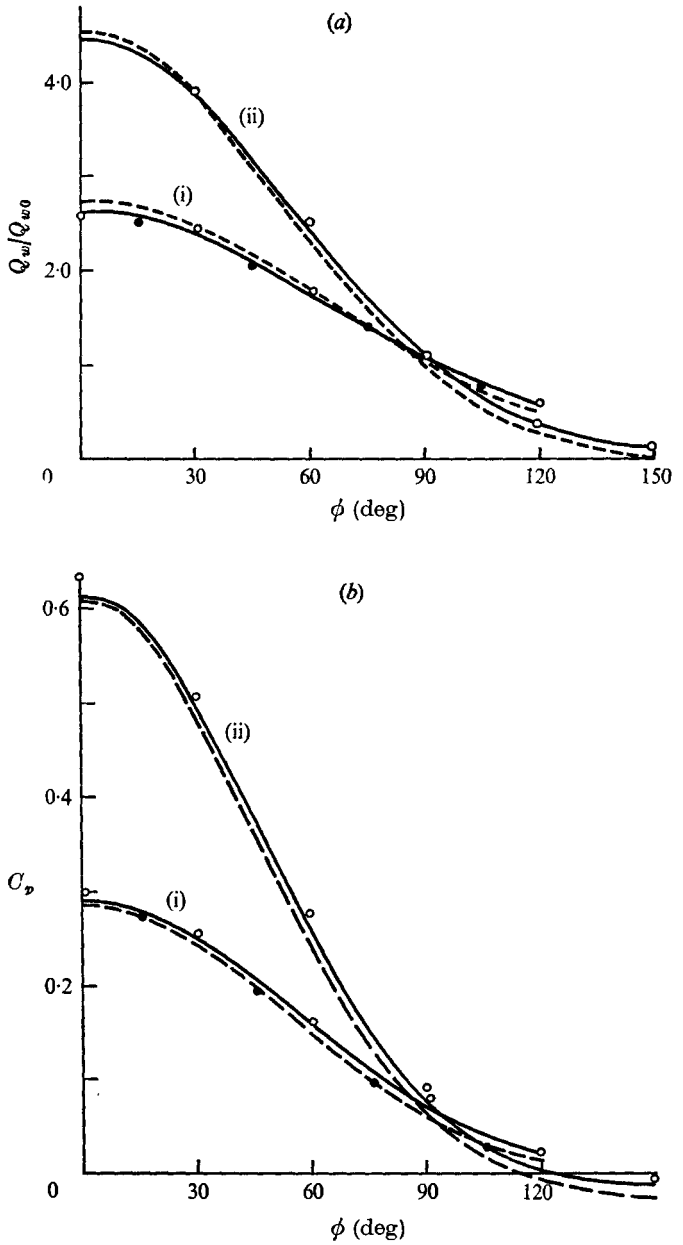

FIGURE 3. Comparison with experiment of (*a*) heat transfer and (*b*) pressure distribution. $M_\infty = 7{\cdot}95, \theta_b = 10°, Re_x = 4{\cdot}2 \times 10^5, T_w/T_0 = 0{\cdot}41$. ———, including displacement-thickness effect; – – – –, excluding displacement-thickness effect; ●, experimental data (Tracy 1963); ○, numerical solution (Lubard & Helliwell 1974), $M_\infty = 8$, $Re_x = 3{\cdot}6 \times 10^5$, $T_w/T_0 = 0{\cdot}41$. (i) $\alpha = 12°$. (ii) $\alpha = 24°$.

(5) The inviscid displacement thickness at the $(i+1)$th mesh point is replaced by

$$\left.\frac{\partial \delta_1^{i+1}}{\partial \zeta}\right|_{\text{inv}} = \left.\frac{\partial \delta_1^*}{\partial \zeta}\right|_{\text{inv}} + k_H \left\{\left.\frac{\partial \delta_1^{i+1}}{\partial \zeta}\right|_{\text{inv}} - \left.\frac{\partial \delta_1^*}{\partial \zeta}\right|_{\text{inv}}\right\}. \tag{5.4}$$

(6) Step 1 is repeated to extrapolate the solution to the $(i+2)$th mesh point, etc.

k_H in (5.4) has been chosen empirically. Most of the results presented have been obtained with $k_H = +1 \times 10^{-4}$. A typical variation of displacement-thickness slope with ϕ is shown in figure 2. The oscillations in $[\partial \delta_1/\partial \zeta]_{\text{visc}}$ at the start ($\phi = 90°$) are due to the small difference between $[\partial \delta_1/\partial \zeta]_{\text{visc}}$ and $[\partial \delta_1/\partial \zeta]_{\text{inv}}$ on the final ray of the windward region. It was found that increasing the number of iterations in the windward region reduced the difference and the oscillations but did not significantly alter the solution. The range of acceptable values of k_H was from approximately $+2 \times 10^{-4}$ to 10^{-5}. Too large a value of k_H caused the early oscillations in $[\partial \delta_1/\partial \zeta]_{\text{visc}}$ to be communicated to $[\partial \delta_1/\partial \zeta]_{\text{inv}}$ and this caused the solution to undergo a divergent oscillation. Too small a value of k_H caused $[\partial \delta_1/\partial \zeta]_{\text{inv}}$ to fail to follow $[\partial \delta_1/\partial \zeta]_{\text{visc}}$ and the solutions smoothly diverged.

The physical effect of not permitting the inviscid–viscous interaction can be seen in the circumferential heat transfer and pressure distributions shown in figure 3. The results at $\alpha = 12°$ represent the lower limit for this method since the method requires a reasonable region of supersonic cross-flow. For these conditions the cross-flow again becomes subsonic soon after 120°. The effect on the heat transfer (Q_{w0} is the heat transfer at $\alpha = 0°$) is qualitatively the same at both $\alpha = 12°$ and 24°. The heat transfer is overpredicted on the windward line of symmetry and underpredicted in the leeward region if no account is taken of the displacement-thickness effect. A similar pattern is obtained at $\alpha = 50°$ (not shown), although the magnitude of the displacement-thickness correction is greater.

The influence on the pressure distribution is not so striking: both the corrected and uncorrected solutions underpredict the experimentally measured pressure distribution. It appears that the improvement to the boundary-layer solution comes from the change in the circumferential derivative of the inviscid solution at the surface rather than the absolute change in the value of the inviscid solution.

The authors are indebted to one referee of the paper for pointing out the possibility (raised by Jones (1968) and Rainbird (1967)) that the difference between theoretical and observed values of the pressure on the windward side may be due to errors in the experimental results.

6. Results

Results are presented here for cone half-angles up to 30° and an incidence range of 12°–50°. Since the inviscid/viscous interaction has little effect on the outer solution, except adjacent to the body, and since inviscid solutions covering the same range of conditions (for free-stream Mach numbers up to 16) have been

presented previously (Fletcher 1974*a*), the present data will be concerned with the behaviour within the boundary layer. Most emphasis will be placed on what happens to the heat transfer, pressure distribution and skin friction at the wall since this is the area of greatest practical significance. Besides obtaining solutions for various incidences and cone angles the effect of changing the Reynolds number and wall temperature has also been examined.

The inviscid results (Fletcher 1975) indicate there is a small leeward shift of the internal shock with increasing Mach number. Since in the real flow the internal shock produces boundary-layer separation it is to be expected that the separation region will contract with increasing Mach number. This result is in agreement with the findings of Lin & Rubin (1973). Since the present method does not explicitly treat the boundary-layer separation the major effect of increasing the free-stream Mach number is to cause an expansion to a slightly lower pressure in the leeward region (Fletcher 1974*a*). Consequently the explicit effect on the total flow of varying the free-stream Mach number has not been considered.

Most of the results presented are for moderate and large angles of attack since the flow behaviour at small and moderate angles of attack has been described previously, e.g. by Lin & Rubin (1973). No attempt has been made to obtain solutions adjacent to the leeward line of symmetry. All solutions are terminated at $\phi = 150°$, which has been chosen to lie beyond the separation angles measured by Avdueskii & Medvedev (1966). However, it is well known from existing experimental studies that the pressure remains constant in the leeward separated region and that the heat transfer and skin friction are substantially constant except for secondary peaks occurring adjacent to the cross-flow vortices which form close to $\phi = 180°$.

The data (complete flow solutions up to $\phi = 150°$) on which this section is based have been obtained on a CDC 7600 and have required approximately 40–60 s for each flow condition. The precise execution time depends on the number of global iterations required in the windward region.

6.1. *Comparison with experiment*

Only a few experimental studies are available of laminar flow including substantial areas of supersonic cross-flow. Among these, Tracy's (1963) provides valuable raw data which can be used as a basis for comparison with theoretical results.

Comparisons of heat transfer and pressure distributions for $\alpha = 12°$ and 24° are shown in figure 3. Agreement, particularly for the heat transfer, is seen to be good once the inviscid/viscous interaction is taken into account. Also shown on the curves for $\alpha = 12°$ are the results of Lubard & Helliwell (1974). Their results appear to underpredict both the heat transfer and the pressure distribution although their test conditions are appropriate to a different Tracy experiment from that considered here.

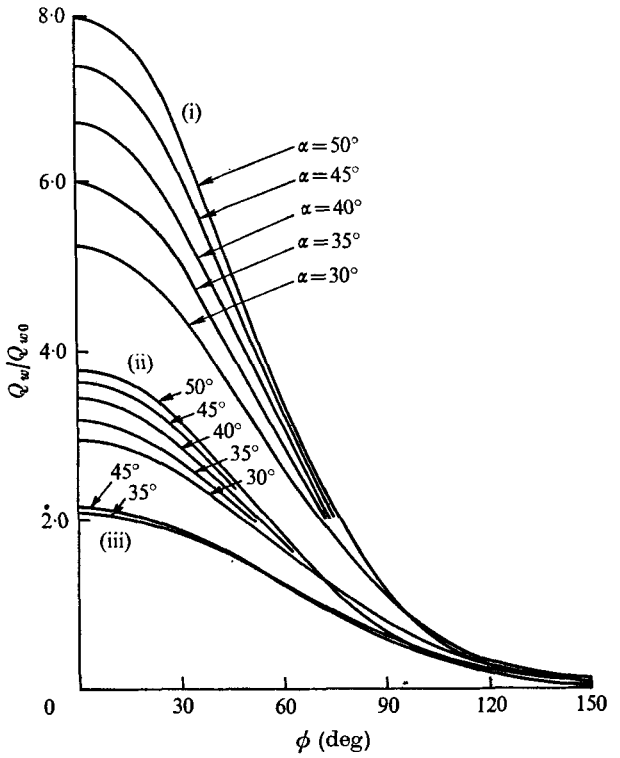

FIGURE 4. Heat-transfer variation with incidence. $M_\infty = 7$, $Re_x = 5 \times 10^5$, $T_w/T_0 = 0{\cdot}40$. (i) $\theta_b = 10°$. (ii) $\theta_b = 20°$. (iii) $\theta_b = 30°$.

6.2. *Effect of incidence and cone angle*

The influence of these two parameters on the heat transfer, pressure distribution and skin friction are shown in figures 4, 5 and 6, respectively. The effect of incidence on the heat transfer for $\theta_b = 10°$ is indicated by curves (i) in figure 4. The major effect occurs in the windward region: an increase in incidence causes a roughly linear increase in heat transfer on the windward line of symmetry. It is interesting that the incidence has an almost negligible effect on the heat transfer in the leeward region. This essentially follows from the almost uniform external (inviscid) conditions and the thick boundary layer in the leeward region.

The behaviour for $\theta_b = 20°$ (curves (ii) in figure 4) is similar in character although the magnitudes of the heat transfer are not so great. The absolute incidences are the same as those indicated for $\theta_b = 10°$, but the relative incidences α/θ_b are smaller. For $\theta_b = 30°$ (curves (iii) in figure 4) only three solutions were obtained (for $\alpha = 35°$, 40° and 48°). No solution is presented for $\alpha = 30°$ because the relative incidence is such that the circumferential extent of the supersonic cross-flow region is very small. A solution was obtained at $\phi = 50°$ but for the rays on and adjacent to the windward line of symmetry the radial velocity component u in the inviscid region was negative, i.e. directed towards the apex of the cone. This would clearly permit communication from the cone base to

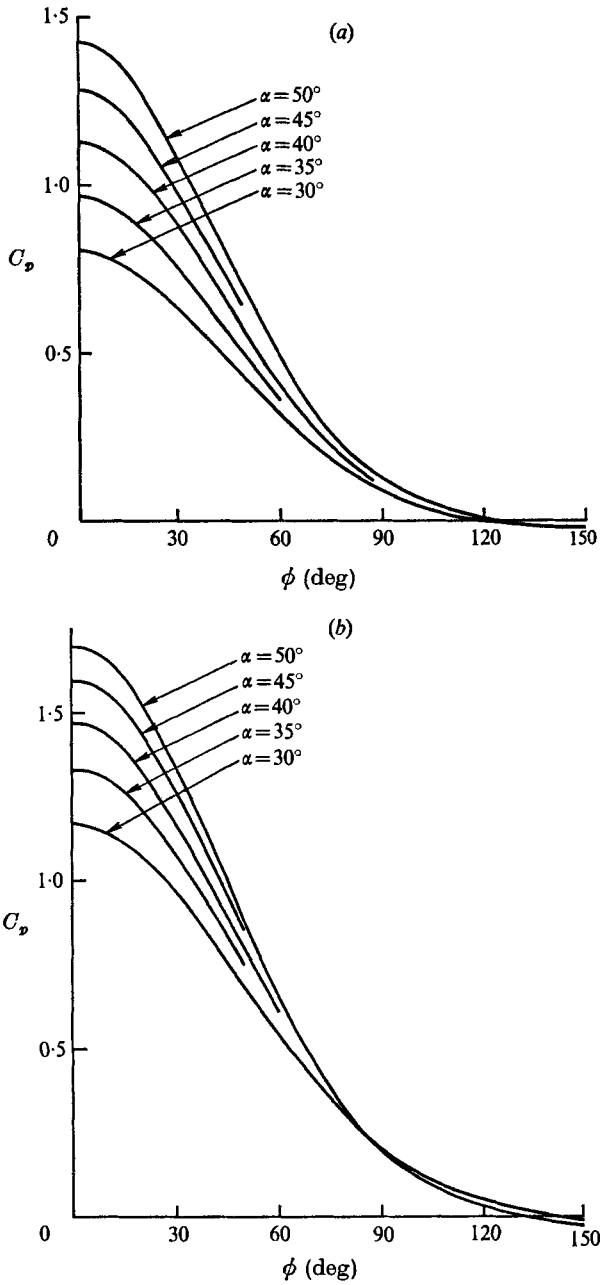

FIGURES 5 (*a*, *b*). For legend see next page.

the cone apex and consequently violate the conical nature of the outer flow. It is assumed that, physically, this set of conditions ($\alpha = 50°, \theta_b = 30°$) would produce a detached shock (one referee of the paper notes that this conclusion is in agreement with the findings of Bachmanova, Lapygin & Lipnitskii 1975). This does not seem surprising when it is realized that the angle of attack of the windward

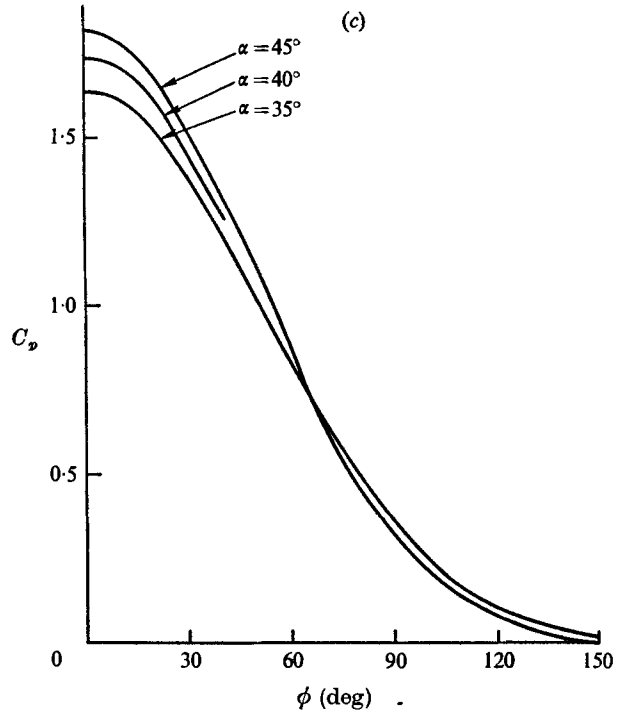

FIGURE 5. Variation of pressure distribution with incidence. $M_\infty = 7$, $Re_x = 5 \times 10^5$, $T_w/T_0 = 0{\cdot}40$. (*a*) $\theta_b = 10°$. (*b*) $\theta_b = 20°$. (*c*) $\theta_b = 30°$.

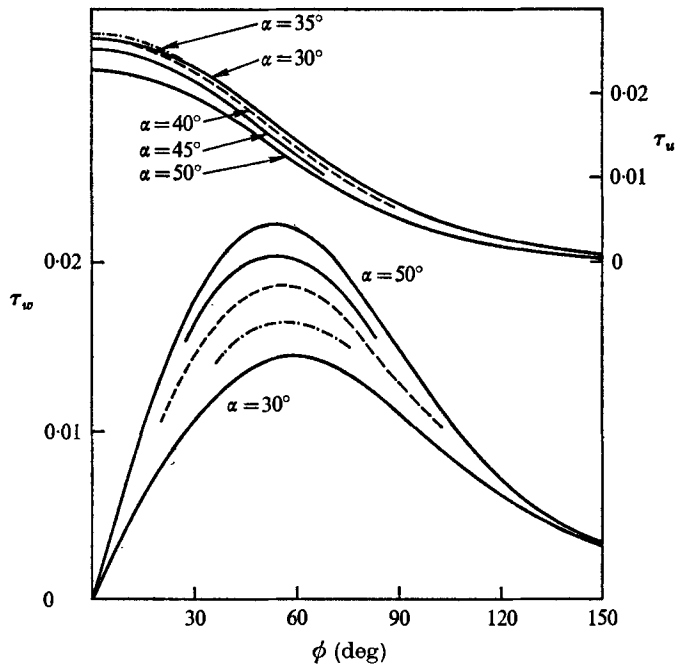

FIGURE 6(*a*). For legend see next page.

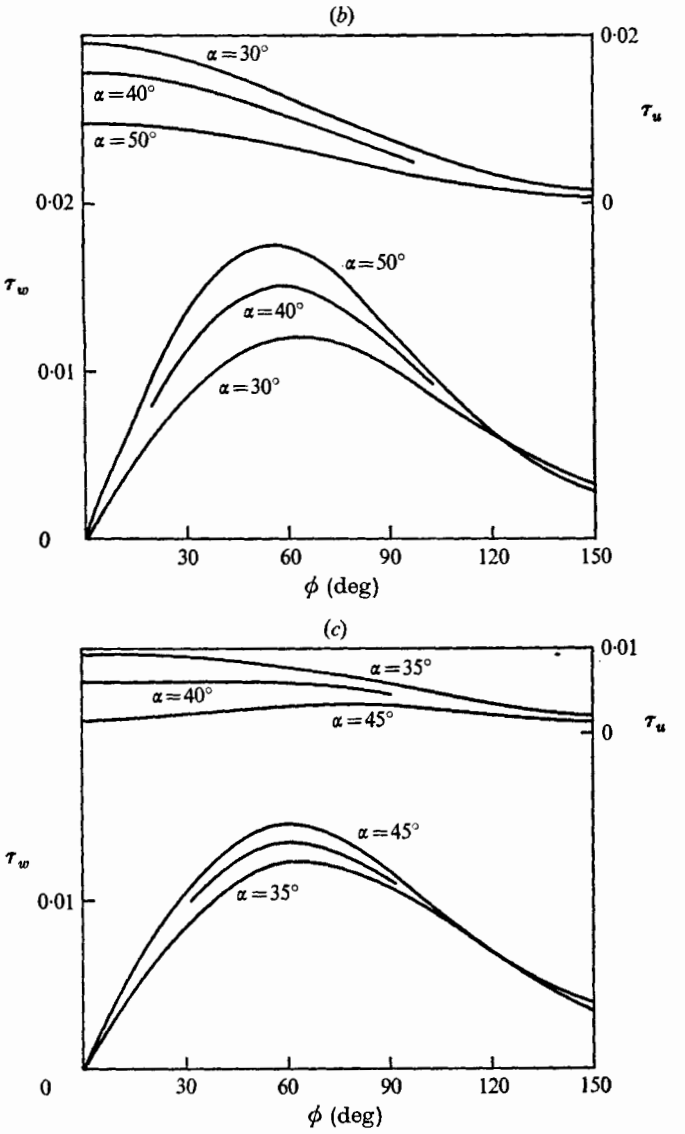

FIGURE 6. Skin-friction variation with incidence. $M_\infty = 7$, $Re_x = 5 \times 10^5$, $T_w/T_0 = 0{\cdot}40$. (*a*) $\theta_b = 10°$. (*b*) $\theta_b = 20°$. (*c*) $\theta_b = 30°$.

line of symmetry is 80°. There is a general tendency for the inviscid radial velocity component u to decrease with increasing nose angle, irrespective of the incidence. Owing to the small range of relative incidence, the variation in heat transfer with angle of attack is very small.

The pressure distributions shown in figure 5 indicate that, as for the heat transfer, most of the variation with incidence occurs on the windward side of the cone. In contrast to the results shown in figure 4, the variation with θ_b indicates that the pressure distribution is not a function of the relative incidence but is a linear function of $\alpha + \theta_b$, at least on the windward line of symmetry. It is

apparent that the pressure in the leeward region is approximately equal to the free-stream value; and this result is independent of both incidence and cone angle.

The skin-friction variation with incidence is shown in figure 6. Because of the large variation of u_e with cone angle the skin-friction results are not presented in coefficient form. τ_u, the radial skin-friction component, and τ_w, the circumferential skin-friction component, are defined as

$$\tau_u = [\mu \partial u/\partial y]_{\text{wall}}, \quad \tau_w = [\mu \partial w/\partial y]_{\text{wall}}.$$

The general behaviour is the same for all the cone angles considered. The radial skin friction falls smoothly from the windward line of symmetry to the leeward region. The only exception to this is the data set for $\alpha = 45°$ and $\theta_b = 30°$, which has a local maximum at approximately $\phi = 85°$. Qualitatively one can consider that the skin friction is determined by two effects. First, τ_u may be expected to increase with ϕ since the inviscid radial velocity component u_e is growing according to $u_{e\phi} = w_e \sin\theta_b$. Second, τ_u may be expected to decrease with ϕ since the boundary-layer thickness is growing with ϕ. For the conditions $\alpha = 45°$, $\theta_b = 30°$ the inviscid radial velocity component u_e is small on the windward line of symmetry (this is consistent with the reversal in u_e at $\alpha = 50°$, $\theta_b = 30°$ as noted above). Thus the rapid growth in u_e is sufficient to overcome the growth in boundary-layer thickness, at least in the windward region.

The circumferential skin-friction component τ_w grows to a maximum at approximately $\phi = 60°$ and then falls smoothly towards the leeward region. As with the heat transfer and pressure distribution, conditions in the leeward region are independent of both incidence and cone angle. The values of τ_w increase approximately linearly with incidence in the windward region. However, the behaviour of τ_u at $\theta_b = 10°$ and $\alpha = 30°$, 35° and 40° does not follow this dependence on incidence. These three results appear to show very small variation with incidence even though the corresponding τ_w variation is conventional.

6.3. *Effect of Reynolds number*

Results are presented for various Reynolds numbers in the range $Re_x = 5 \times 10^4$ to 10^6. The upper limit has been imposed as the approximate limit of laminar flow. In order to ascertain any cross-coupling effect the Reynolds number variation has been considered for two different conditions: moderate incidence ($\alpha = 30°$, $\theta_b = 20°$) and large incidence ($\alpha = 50°$, $\theta_b = 10°$). All results have been obtained at $M_\infty = 7$ and $T_w/T_0 = 0{\cdot}40$. The variation of the heat transfer, circumferential skin friction and displacement thickness are shown in figures 7, 8 and 9, respectively. The effect of Reynolds number on the pressure distribution is small and is not shown.

The heat-transfer results (figure 7) indicate that the major effect of Reynolds number occurs in the windward region close to the windward line of symmetry. An increase in Reynolds number causes a small increase in heat transfer owing essentially to the reduction in boundary-layer thickness. This is more apparent at large incidence. A reversal in the variation with Reynolds number is apparent in the leeward region, although the variation is small.

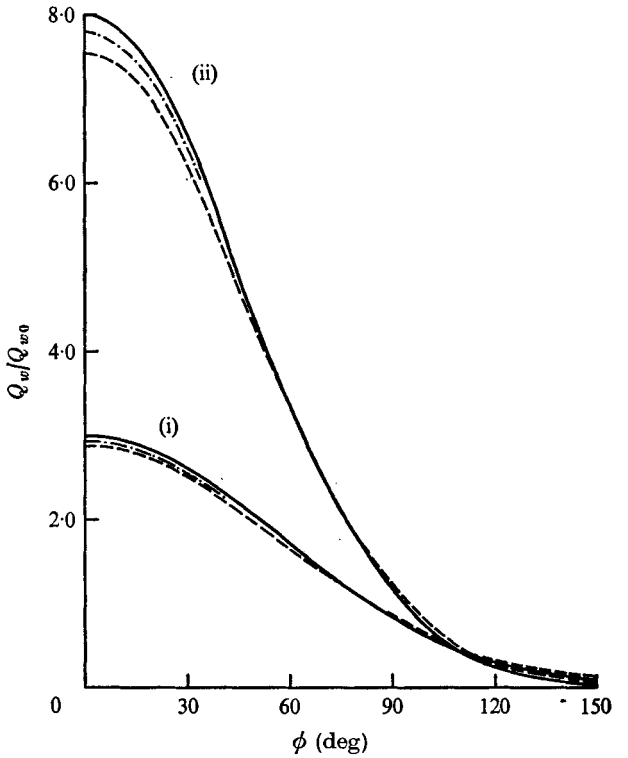

FIGURE 7. Heat-transfer variation with Reynolds number. $M_\infty = 7$, $T_w/T_0 = 0{\cdot}40$. (i) Moderate incidence, $\alpha = 30°$, $\theta_b = 20°$. (ii) Large incidence, $\alpha = 50°$, $\theta_b = 10°$. ———, $Re_x = 10^6$; – · – · –, $Re_x = 2 \times 10^5$; – – – – –, $Re_x = 5 \times 10^4$.

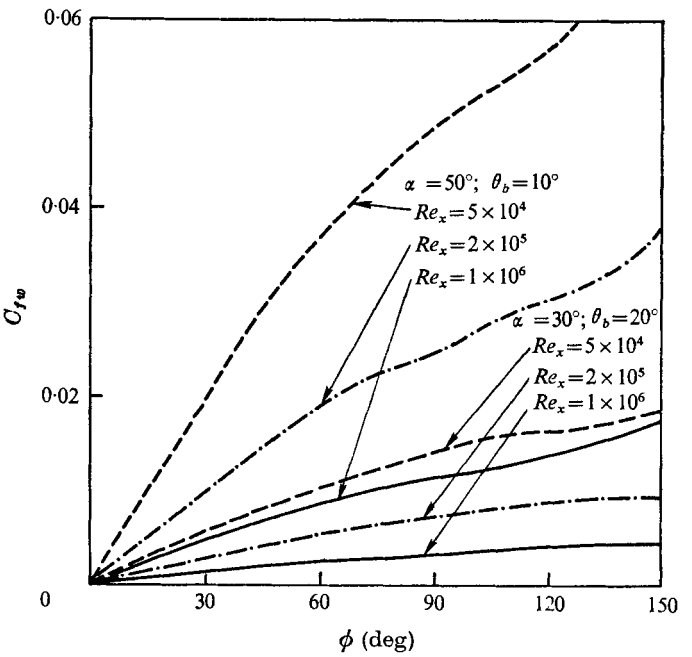

FIGURE 8. Circumferential skin-friction variation with Reynolds number. $M_\infty = 7$, $T_w/T_0 = 0{\cdot}40$.

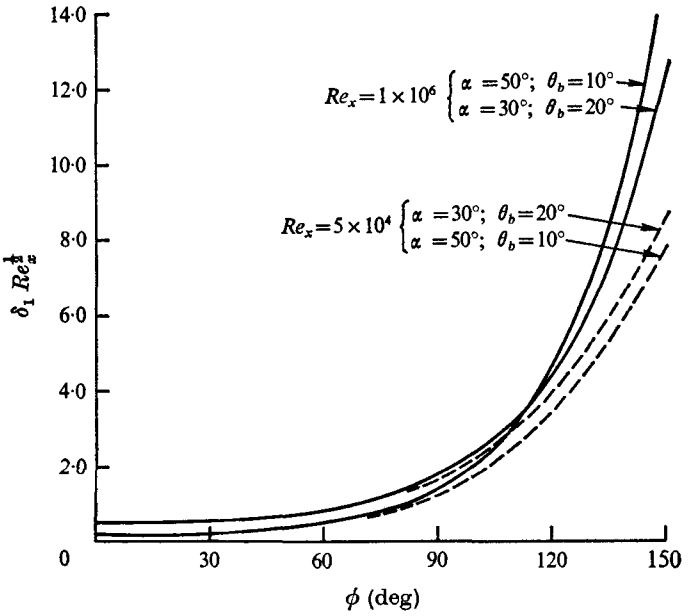

FIGURE 9. Displacement-thickness variation with Reynolds number. $M_\infty = 7$, $T_w/T_0 = 0{\cdot}40$.

The circumferential skin-friction coefficient C_{fw} is defined as $C_{fw} = \tau_w/\frac{1}{2}\rho_e u_e^2$. The results shown in figure 8 indicate a monotonic increase in C_{fw} with ϕ. Comparing this result with the variation of τ_w shown in figure 6, it is apparent that the continued increase in C_{fw} with ϕ in the leeward region is due to the rapid decrease in ρ_e. Since $u_{e\phi} = w_e \sin\theta_b$, $u_{e\phi}$ is positive for all ϕ considered. An increase in Reynolds number causes a fall in C_{fw}; the effect is greater at the larger incidence. The variation of C_{fu} with Reynolds number is qualitatively the same but the changes are smaller.

In order to collapse the results for the displacement-thickness variation with Reynolds number the similarity parameter $Re_x^{\frac{1}{2}}$ has been introduced into figure 9. In the windward region the results for all Reynolds numbers collapse onto a single curve at a given incidence or cone angle. In contrast, the similar behaviour breaks down in the leeward region, where the results tend to group themselves according to Reynolds number irrespective of incidence or cone angle.

6.4. *Effect of surface temperature*

A range of surface temperature ratios T_w/T_0 from 0·1 to 0·9 has been considered. As in §6.3, the effect of moderate ($\alpha = 30°$, $\theta_b = 20°$) and large ($\alpha = 50°$, $\theta_b = 10°$) incidence has been obtained. All results presented in this section have been obtained at $M_\infty = 7$ and $Re_x = 5 \times 10^5$. No attempt has been made to obtain solutions corresponding to an adiabatic wall; this could be done but would require a different treatment of the wall boundary condition on s (see §4.2). The results for a hot wall, $T_w/T_0 = 0{\cdot}9$ (see figure 10), approximate this case.

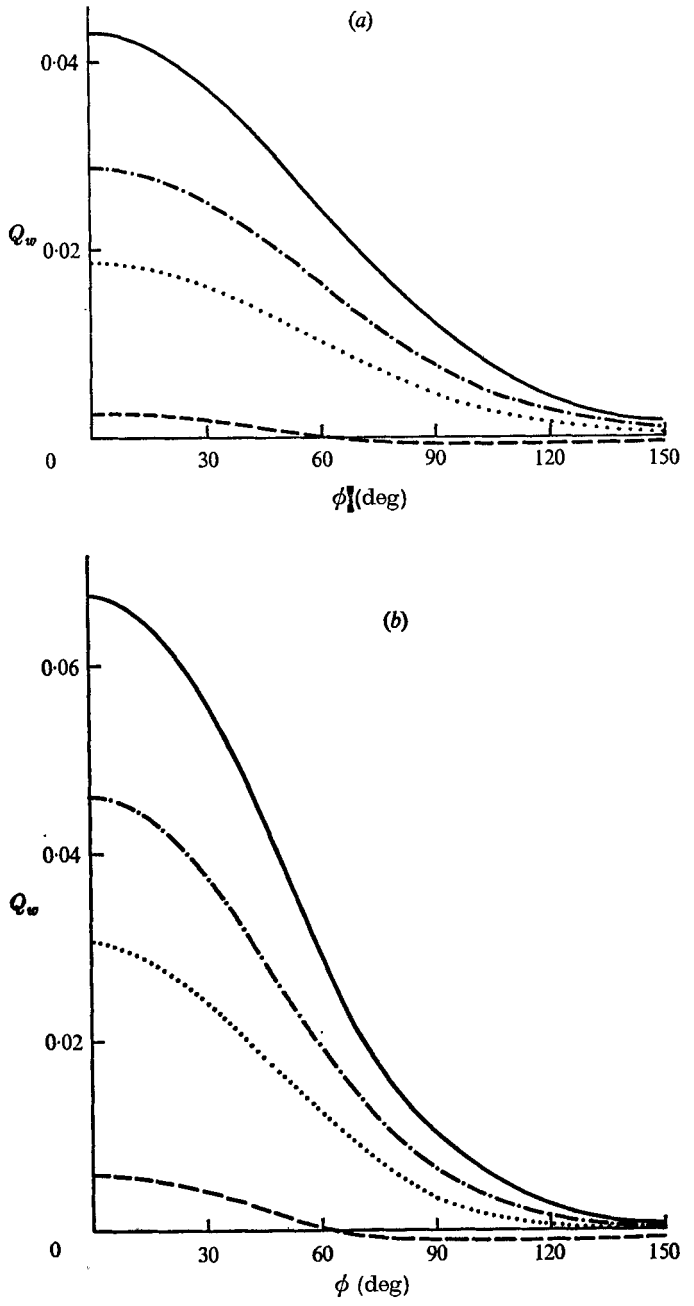

FIGURE. 10. Heat-transfer variation with wall temperature ratio. $M_\infty = 7$, $Re_x = 5 \times 10^5$. (*a*) Moderate incidence, $\alpha = 30°$, $\theta_b = 20°$. (*b*) Large incidence, $\alpha = 50°$, $\theta_b = 10°$. ———, $T_w/T_0 = 0{\cdot}1$; – · – · – · , $T_w/T_0 = 0{\cdot}4$; · · · · · , $T_w/T_0 = 0{\cdot}6$; – – – – –, $T_w/T_0 = 0{\cdot}9$.

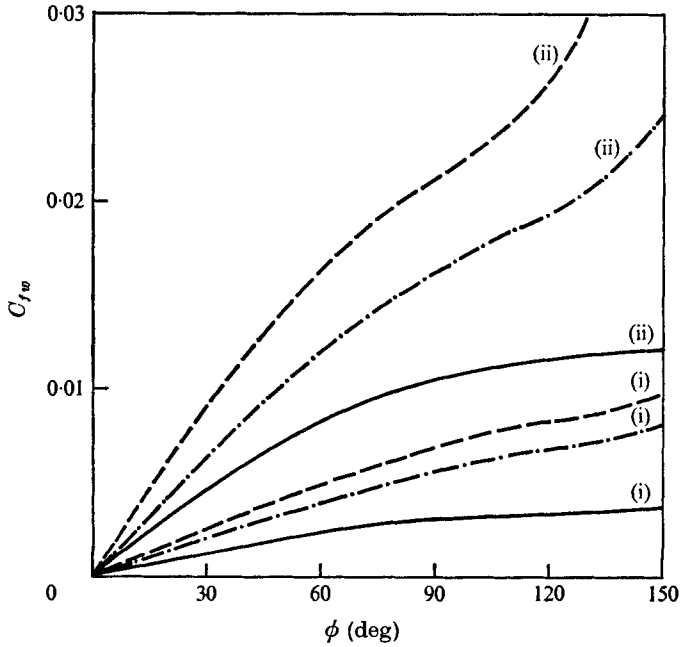

FIGURE 11. Circumferential skin-friction variation with wall temperature ratio. $M_\infty = 7$, $Re_x = 5 \times 10^5$. (i) Moderate incidence, $\alpha = 30°$, $\theta_b = 20°$. (ii) Large incidence, $\alpha = 50°$, $\theta_b = 10°$. ———, $T_w/T_0 = 0{\cdot}1$; - · - · -, $T_w/T_0 = 0{\cdot}4$, – – – –, $T_w/T_0 = 0{\cdot}9$.

The results for the heat transfer (figure 10) are not expressed as a ratio to the corresponding zero-incidence results Q_{w0} because for $T_w/T_0 = 0{\cdot}9$, Q_{w0} changes sign at an intermediate ϕ and this would cause a spurious effect. The results shown in figure 10 demonstrate a general trend of reducing heat transfer as the wall temperature ratio increases. This effect is greater for the larger incidence and, as with all the other variables considered so far, is essentially confined to the windward region. The variation of heat transfer with temperature ratio in the leeward region is very small.

The variation of the circumferential skin-friction coefficient C_{fw} with ϕ is illustrated in figure 11. The effect of increasing the wall temperature ratio causes an increase in C_{fw} for all ϕ and for both moderate and large incidence. The effect is magnified at large incidence. The cold-wall results ($T_w/T_0 = 0{\cdot}1$) indicate that C_{fw} is approaching a limit as ϕ increases in the leeward region, whereas increasing the wall temperature produces a continuing growth of C_{fw} with ϕ.

The effect of wall temperature on the temperature distribution within the boundary layer is shown in figure 12. The results for the larger incidence (figure 12*b*) were obtained at $\phi = 82{\cdot}5°$. The results are qualitatively independent of incidence and all the results (with the exception of the hot-wall case, $T_w/T_0 = 0{\cdot}9$) show an increase in temperature as a traverse is made from the wall to the inviscid region. A rapid adjustment takes place close to the wall, followed by a more gradual adjustment to the inviscid conditions as the outer edge of the boundary layer is approached.

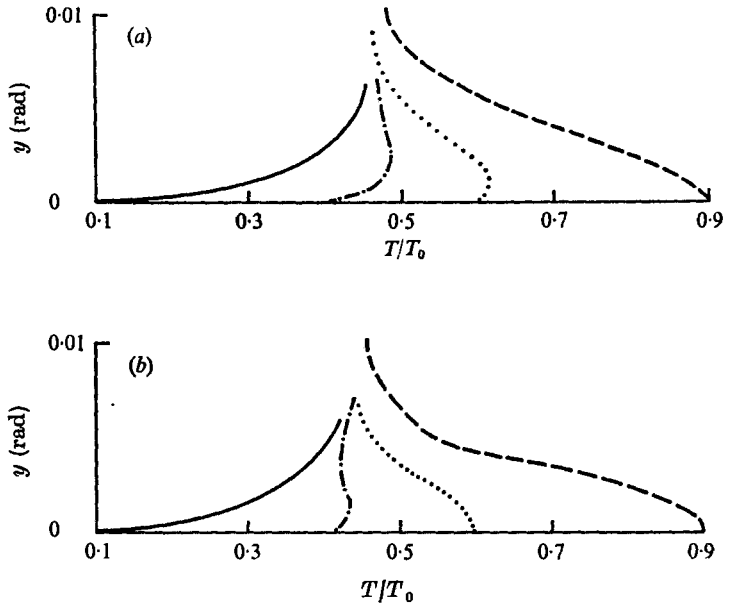

FIGURE 12. Temperature variation with wall temperature ratio. $M_\infty = 7$, $Re_x = 5 \times 10^5$. (*a*) Moderate incidence, $\alpha = 30°$, $\theta_b = 20°$. (*b*) Large incidence, $\alpha = 50°$, $\theta_b = 10°$. ———, $T_w/T_0 = 0{\cdot}1$; – · – · –, $T_w/T_0 = 0{\cdot}4$; · · · · · ·, $T_w/T_0 = 0{\cdot}6$; – – – – –, $T_w/T_0 = 0{\cdot}9$.

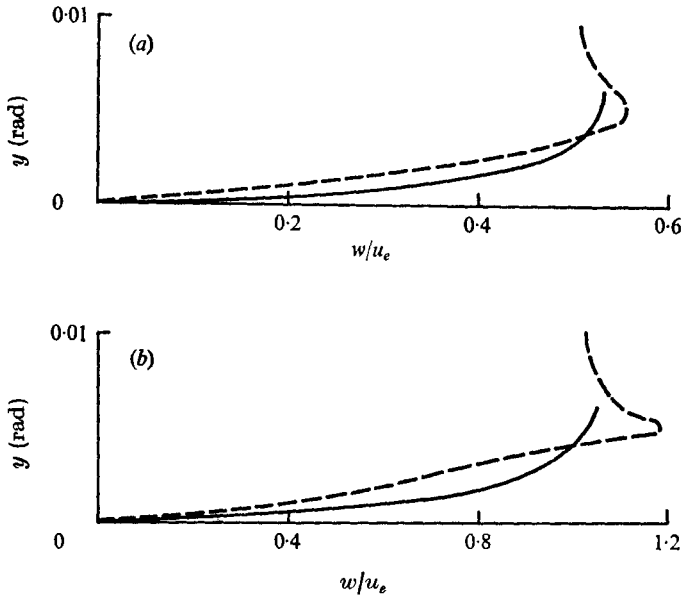

FIGURE 13. Circumferential velocity variation with wall temperature ratio. $M_\infty = 7$, $Re_x = 5 \times 10^5$. (*a*) Moderate incidence, $\alpha = 30°$, $\theta_b = 20°$. (*b*) Large incidence, $\alpha = 50°$, $\theta_b = 10°$. ———, $T_w/T_0 = 0{\cdot}1$; – – – – –, $T_w/T_0 = 0{\cdot}9$.

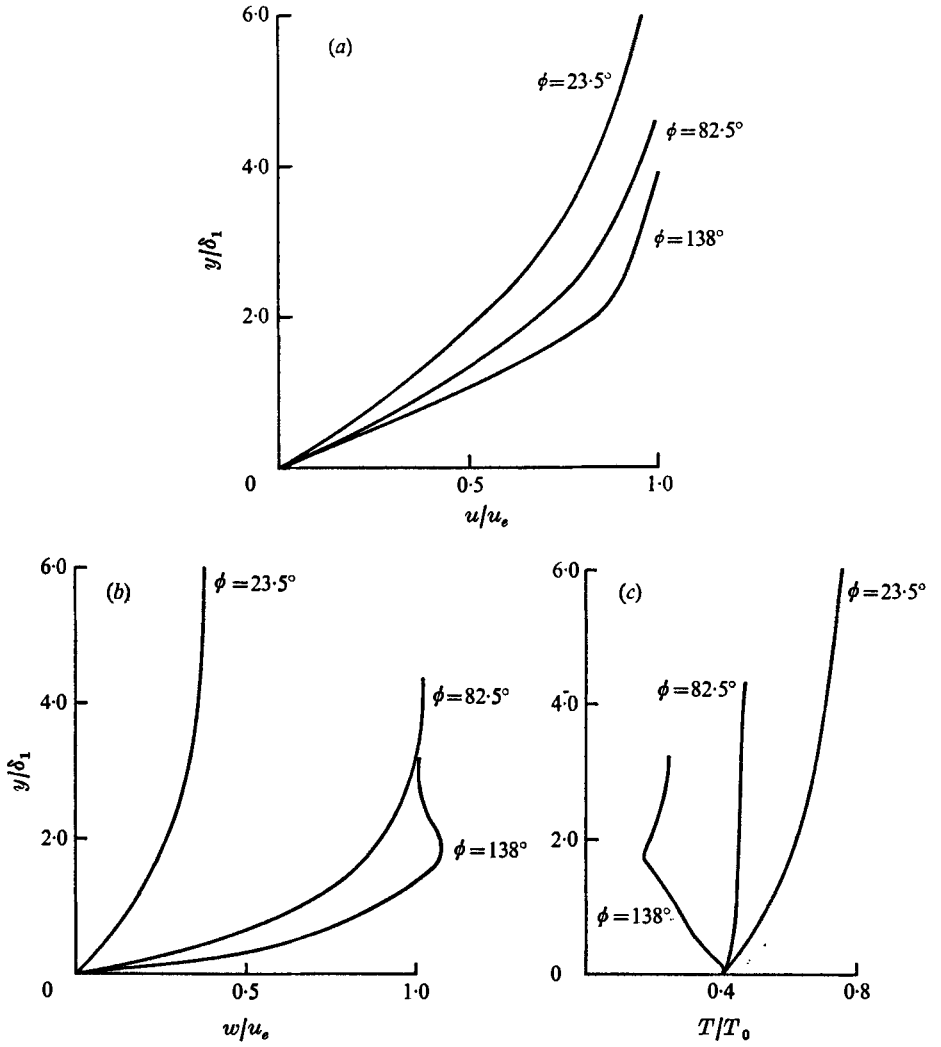

FIGURE 14. Boundary-layer profiles. $M_\infty = 7$, $\alpha = 50°$, $\theta_b = 10°$, $Re_x = 5 \times 10^5$, $T_w/T_0 = 0{\cdot}4$. (*a*) Radial velocity component. (*b*) Circumferential velocity component. (*c*) Temperature.

The corresponding variation in the circumferential velocity component is shown in figure 13. Only results corresponding to the extreme temperature ratios are shown. The case of a nearly adiabatic wall ($T_w/T_0 = 0{\cdot}9$) produces an interesting local maximum within the boundary layer. The results for moderate and large incidence are qualitatively the same.

6.5. *Velocity and temperature profiles*

For a large angle of attack ($\alpha = 50°$, $\theta_b = 10°$) the variation of the velocity and temperature profiles with circumferential location are presented in figure 14. In order to reduce the spread of the results the normal co-ordinate has been

scaled by the local displacement thickness. Comparison of figures 14(*a*) and 9 indicates that a plot of y (rad) *vs.* u/u_e would cause the results in figure 14(*a*) to occur in reverse order.

The variation of the axial velocity component u with ϕ is not very great, as indicated by figure 14(*a*). There is a general steepening of the profile as ϕ increases. The w profiles (figure 14*b*) demonstrate a tendency to develop a local maximum as ϕ increases. This effect is also apparent in the moderate incidence results of Dwyer (1971) and Lin & Rubin (1973). Comparing figure 14(*a*) with figure 13, it is apparent that increasing the wall temperature causes the local maximum in w to appear at smaller ϕ.

The temperature variation with increasing ϕ is shown in figure 14(*c*). Even at the largest ϕ (138°), where the inviscid temperature is less than the wall temperature, there is still a net flow of heat to the wall. The local minimum in temperature at an intermediate point in the boundary layer (at $\phi = 138°$) is associated with the local maximum in the circumferential velocity component (figure 14*b*).

7. Conclusion

The present results extend previous investigations (e.g. Lin & Rubin 1973) to larger incidences (up to 50°) and cone angles (up to 30°) and show the systematic variation with Reynolds number and wall temperature ratio. By considering the effect of these parameters on the conditions at the body surface, i.e. the heat transfer, pressure distribution and skin friction, the following conclusions may be drawn.

(i) The behaviour at large incidence and cone angle is qualitatively the same as that at moderate incidence and small cone angle.

(ii) Variations in surface conditions caused by varying the above parameters are confined to the windward region.

(iii) Once the inviscid cross-flow is supersonic conditions at the surface in the leeward region are virtually independent of any of the parameter changes considered above. This situation is not expected to be greatly altered in the leeward separated region.

(iv) The result of permitting the displacement-thickness effect to modify the outer inviscid solution causes a small, but significant change in conditions at the surface, particularly the heat transfer.

(v) The present technique can in principle be extended to the far windward region provided numerical integration of the right sides of (2.20)–(2.22) is replaced by an algebraic calculation, outlined in §4.3.

REFERENCES

AVDUEVSKI, V. S. & MEDVEDEV, K. I. 1966 *Izv. Akad. Nauk SSSR Mekh. Zh. i Gaza*, **3**, 117–119.

BABENKO, K. I., VOZKRESENSKII, G. P., LYUBIMOV, A. N. & RUSANOV, V. V. 1964 *Akad. Nauk SSSR Matem. im V. A. Steklova, Moscow.* (See also *N.A.S.A.* TT F-380, 1966.)

BACHMANOVA, N. S., LAPYGIN, V. I. & LIPNITSKII, YU. M. 1975 *Fluid Dyn.* **8**, 915–919.

BASHKIN, V. A. 1968 *Zh. Vychisl. Mat. Mat. Fiz.* **8**, 1280–1290.

BAZZHIN, A. P. 1971 *Proc. 2nd Int. Conf. on Numerical Methods in Fluid Dyn. Lecture Notes in Physics*, vol. 8 (ed. M. Holt), pp. 223–229. Springer.

BELOTSERKOVSKII, O. M. & CHUSHKIN, P. I. 1965 In *Basic Developments in Fluid Dynamics* (ed. M. Holt), vol. 1, pp. 89–128. Academic.

BOERICKE, R. R. 1971 *A.I.A.A. J.* **9**, 462–468.

DWYER, H. A. 1971 *A.I.A.A. J.* **9**, 277–284.

FLETCHER, C. A. J. 1974*a* *University of California at Berkeley Rep.* FM-74-8.

FLETCHER, C. A. J. 1974*b* *Proc. 4th Int. Conf. on Numerical Methods in Fluid Dyn. Lecture Notes in Physics*, vol. 35 (ed. R. D. Richtmyer), pp. 161–166. Springer.

FLETCHER, C. A. J. 1975 *A.I.A.A. J.* **13**, 1073–1078.

FLETCHER, C. A. J. & HOLT, M. 1975 *J. Comp. Phys.* **18**, 154–164.

GEAR, C. W. 1971 *Comm. A.C.M.* **14**, 176–179.

GILINSKII, S. M., TELENIN, G. F. & TINYAKOV, G. P. 1964 *Izv. Akad. Nauk SSR, Mechan. i mashinostr.* **4**, 9–28. (see also *N.A.S.A.* TT F-297, 1965.)

HOLT, M. & NDEFO, D. E. 1970 *J. Comp. Phys.* **5**, 463–486.

JONES, D. J. 1968 *Nat. Res. Counc. Can. Aero. Rep.* LR-507.

KUTLER, P. & LOMAX, H. 1970 *Proc. 2nd Int. Conf. on Numerical Methods in Fluid Dyn. Lecture Notes in Physics*, vol. 8 (ed. M. Holt), pp. 24–29. Springer.

LIN, T. C. & RUBIN, S. G. 1973 *J. Fluid Mech.* **59**, 593–620.

LUBARD, S. & HELLIWELL, W. S. 1974 *A.I.A.A. J.* **12**, 965–974.

MARCILLAT, J. & ROUX, B. 1972 *A.I.A.A. J.* **10**, 1625–1630.

MOORE, F. K. 1951 *N.A.C.A. Tech. Note*, no. 2279.

MOORE, F. K. 1952 *N.A.C.A. Tech. Note*, no. 2722.

POWELL, M. J. D. 1964 *Comp. J.* **7**, 303–307.

RAINBIRD, W. J. 1967 *Nat. Res. Counc. Can. DME/NAE Quart. Bull.* no. 1967(3).

RAINBIRD, W. J. 1968 *AGARD Conf. Proc.* no. 30, paper 30.

TRACY, R. R. 1963 *California Inst. Tech. Memo.* no. 69.

YAHALOM, R. 1971 *University of California at Berkeley, Rep.* AS-71-2.